Accepted Manuscript

Title: RGD-Functionalized Fe_3O_4 Nanoparticles for Magnetic Hyperthermia

Authors: Oihane K. Arriortua, Maite Insausti, Luis Lezama, Izaskun Gil de Muro, Eneko Garaio, Jesus Martínez de la Fuente, Raluca M. Fratila, Maria P. Morales, Rocío Costa, Maite Eceiza, Maialen Sagartzazu-Aizpurua, Jesus M. Aizpurua

PII: S0927-7765(18)30106-1
DOI: https://doi.org/10.1016/j.colsurfb.2018.02.031
Reference: COLSUB 9171

To appear in: *Colloids and Surfaces B: Biointerfaces*

Received date: 13-11-2017
Revised date: 31-1-2018
Accepted date: 14-2-2018

Please cite this article as: Oihane K.Arriortua, Maite Insausti, Luis Lezama, Izaskun Gil de Muro, Eneko Garaio, Jesus Martínez de la Fuente, Raluca M.Fratila, Maria P.Morales, Rocío Costa, Maite Eceiza, Maialen Sagartzazu-Aizpurua, Jesus M.Aizpurua, RGD-Functionalized Fe3O4 Nanoparticles for Magnetic Hyperthermia, Colloids and Surfaces B: Biointerfaces https://doi.org/10.1016/j.colsurfb.2018.02.031

RGD-Functionalized Fe_3O_4 Nanoparticles for Magnetic Hyperthermia

Oihane K. Arriortua,[a] Maite Insausti,[a,b]* Luis Lezama,[a,b] Izaskun Gil de Muro,[a,b] Eneko Garaio,[c] Jesus Martínez de la Fuente,[d] Raluca M. Fratila,[d] Maria P. Morales,[e] Rocío Costa,[e] Maite Eceiza,[f] Maialen Sagartzazu-Aizpurua[f] and Jesus M. Aizpurua[f]

[a] BC Materials, Basque Center for Materials, Applications & Nanostructures, 48610, Derio, Spain.

[b] Inorganic Chemistry, Department University of Basque Country, 48940, Leioa, Spain

[c] Electricity and Electronic Department, University of Basque Country, 48940, Leioa, Spain

[d] Group of Biofunctional Nanoparticles and Surfaces, Instituto de Nanociencia de Aragón, 50018, Zaragoza, Spain

[e] Biomaterials and Bioinspired Materials Department, Instituto de Ciencia de Materiales de Madrid, ICMM-CSIC, 28049, Madrid, Spain

[f] José Mari Korta R&D Center, Basque Country University, UPV/EHU, 20018, Donostia, Spain

*Corresponding author should be addressed. E-mail: maite.insausti@ehu.es

Graphical Abstract

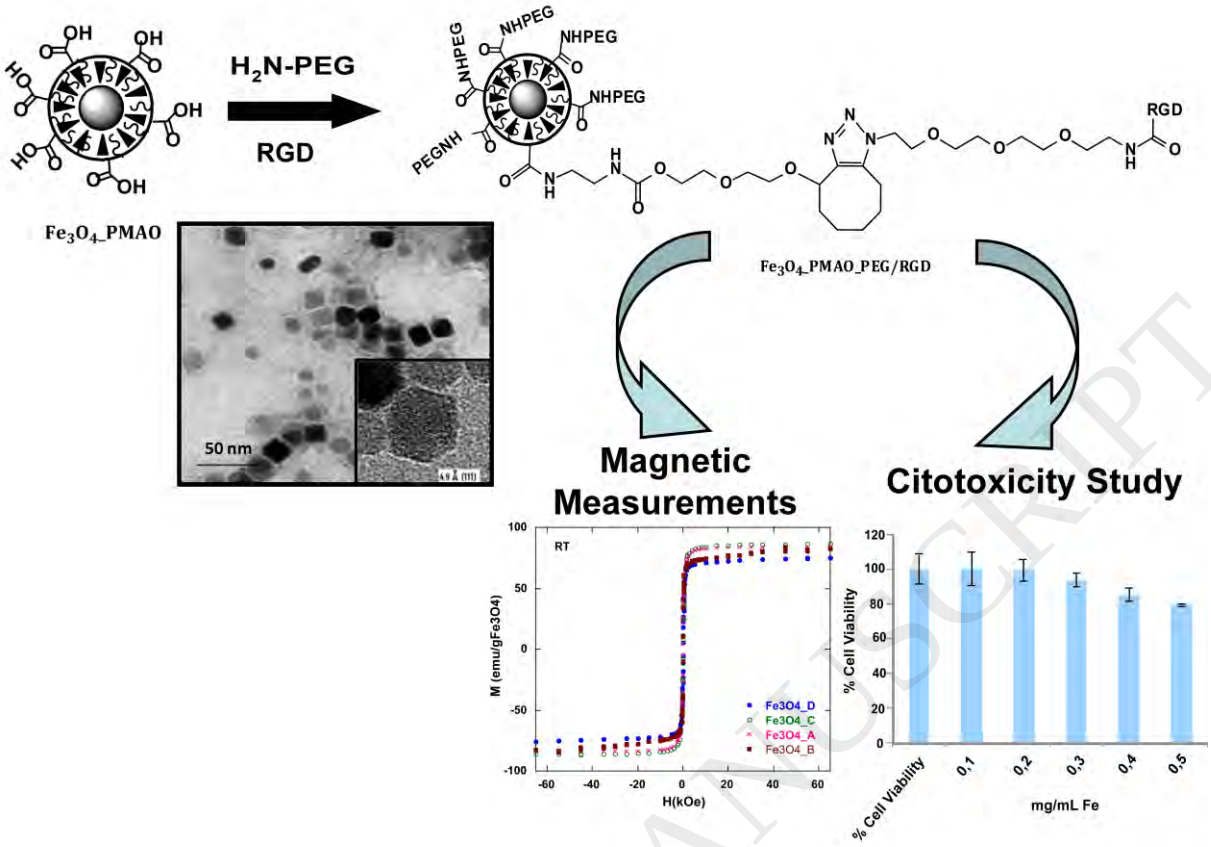

HIGHLIGHTS

- Thermal decomposition by successive additions allows obtaining magnetite
- particles of 11 - 23 nm.
- Preparation of water souble Nps by recovering with PMAO, DMSA and
- TESPMA ligands.
- Fe_3O_4@PMAO nanoparticles display high values of SAR, increasing with the
- size of the NP.
- RGD peptides have been targeted to Fe_3O_4@PMAO NPs by “click” chemistry.
- Fe_3O_4@PMAO@PEG/RGD NPs exhibit nontoxicity in “in vitro” assays.

ABSTRACT:

To improve the selectivity of magnetic nanoparticles for tumor treatment by hyperthermia, Fe_3O_4 nanoparticles have been functionalized with a peptide of the type arginine-glycine-aspartate (RGD) following a “click” chemistry approach. The RGD peptide was linked onto the previously coated nanoparticles in order to target $\alpha_v\beta_3$ integrin receptors over-expressed in angiogenic cancer cells. Different coatings have been analyzed to enhance the

biocompatibility of magnetic nanoparticles. Monodispersed and homogeneous magnetite nanoparticles have been synthesized by the seed growth method and have been characterized using X-ray diffraction, thermogravimetric analysis, infrared spectroscopy, transmission electron microscopy and magnetic measurements. The magnetic hyperthermia efficiency of the nanoparticles has also been investigated and cytotoxicity assays have been perfomed for functionalized nanoparticles.

Keywords: Magnetite• RGD •EMR • Citotoxicity • Hyperthermia

1. Introduction

In recent years, the study of magnetic nanoparticles (MNPs) targeting specific biological tissues to elicit predetermined responses has become an important platform in the diagnosis and treatment of certain diseases [1]. Indeed, the combination of such selectivity with the application of an alternating magnetic field represents a novel therapeutic approach to treat cancer by means of magnetic hyperthermia [2]. The

energy dissipated in such process can be represented by the specific power adsorption rate (*SAR*) which, apart from the characteristics of the external alternating electromagnetic current (AC) applied, depends on a number of critical properties of MNPs, such as saturation magnetization, magnetic anisotropy, size, or colloidal stability [3-4]. From the experimental point of view, the way to find the best compromise of all these factors is constrained by the ability to produce custom designed MNPs displaying strong magnetic response, together with high tumor tissue-affinity and lack of toxicity [5,6]. The reliable production of such properly tuned MNPs represents a major challenge nowadays.

Among the magnetic materials, magnetite is usually employed because of its high saturation magnetization, high remanence and moderate anisotropy constant, good biocompatibility and low citotoxicity [7]. In order to synthesize magnetite nuclei under reproducible conditions, nonaqueous approaches are usually followed as nucleation and growth processes are well separated, providing control over the size, crystallinity and shape of nanoparticles [8]. These approaches provide magnetite nanoparticles surrounded by a shell of hydrophobic ligand molecules, which can be replaced with hydrophilic molecules or coated with amphiphilic polymers to render the nanoparticles water soluble. Dextran [9,10], chitosan [11,12], PEG [13,14] or aminoalkylsilanes [15,16] have been employed with this purpose, but poor stability is often attained. The polymeric amphiphilic ligand poly(maleic anhydride-alt-1-octadecene) (PMAO) presents a proper option as interacts with the hydrophobic surface of the nanoparticle by intercalating its 16-carbon-long alkyl chains, leaving the hydrophilic portion of the polymer exposed to the solution [17].

To enhance the selective binding of nanoparticles to bioreceptors, an additional functionalization of their surface is often required [18,19]. Targeting can be accomplished by coupling onto the NP a homing element, such as an antibody or peptide that specifically binds to the target tissue [20]. One of the most widely studied adhesive peptide in the biomaterials field is the tri-amino acid sequence arginine-glycine-aspartate (RGD) [21]. This sequence can bind to multiple integrin species such as $\alpha_\beta v_3$ and $\alpha_\beta v_5$, which are usually overexpressed in tumor endothelia [22]. RGD can be further modified to incorporate anchoring groups, such as azides or amines, and also tagging groups like fluorophores [23]. This approach aims to combine two major

advantages for the hyperthermia treatment: high local nanoparticle concentration at the site of the disease process and low systemic exposure.

Among the chemical strategies to bind peptides to the surface of nanoparticles, "click chemistry" [24,25] displays unique features such as full aqueous compatibility, high chemical orthogonality and wide substrate tolerance. More particularly, the copper-catalyzed [3+2]-dipolar cycloaddition of azides with terminal alkynes [26], in combination with conventional bioconjugation [27] strategies, provides a general access to multifunctional nanobiomaterials. Within this context, the copper-free version of the reaction conducted with strain-activated cyclooctynes, constitutes the strategy of choice for "in vivo" applications [28,29].

In this paper a seed growth method has been employed for a fine-tuning of particle sizes and good mono-dispersity [30,31]. A fine adjustment of the synthetic conditions allows for obtaining oleic acid and oleylamine capped magnetite nanoparticles with defined shapes and sizes [32]. These iron oxide nanoparticles dispersed in organic medium have been transferred into aqueous phase by ligand interchange using dimercaptosuccinic acid (DMSA) [33], N-(triethoxysilylpropyl)-maleamic acid (TESPMA) [34] and by adding poly(maleic anhydride-alt-1-octadecene) (PMAO) [35]. The free carboxylic groups in the coated polymer have been activated for "click" reactivity via amide coupling with the hydrophilic w-aminoalkylcyclooctine 10-(2-cyclooctyn-1-oxy)-3-aza-5,8-dioxa-4-oxodecyl-1-amine. Finally, the resulting nanoparticles have been clicked to the azide-modified RGD derivative H-Arg-Gly-Asp-NH$(CH_2CH_2O)_3CH_2CH_2N_3$ under copper-free conditions [36]. Since the ultimate application of these nanoparticles was the treatment of liver cancer tumors by magnetic hyperthermia, *SAR* measurements were accomplished in order to spot the nanoparticles with a better response, lower cytotoxicity and better biocompatibility. These results are presented together with an exhaustive study of the magnetic properties of the samples by means of magnetization measurements and Electron Magnetic Resonance (EMR). This last powerful microscopic tool can provide useful information on particle size evaluation, shape and surface effects or inter-particle interactions [37,38].

2. Materials and methods

2.1. Materials

All reagents and solvents were obtained from commercial sources and were used without further purification unless stated otherwise. 1,2-Hexadecanediol (90%), dibenzyl ether (98%), toluene (99,5%), dimethyl sulfoxide (DMSO, 99.9%), poly-(maleic anhydride-alt-1-octadecene) (PMAO, 30.000-50.000 g/mol), HOBt and trifluoroacetic acid, dimercaptosuccinic acid (DMSA, 98%), tetrahydrofuran (THF, 99%), acetic acid (AcOH, 99%), (N-(3-dimethylaminopropyl)-N′-ethylcarbodiimide hydrochloride (EDC, 99%), polyethyleneglycol methyl ether amine (PEG-NH_2, Pm□□ 500g/mol) and N,N'-disuccinimidyl carbonate (DSC) were purchased from Sigma-Aldrich. Iron (0) pentacarbonyl (99%) and oleylamine (80-90%) were from Acros, oleic acid (100%) from Fluka and ethanol (96%), sodium hydroxide (98%) and trichloromethane stabilized with ethanol PA ($CHCl_3$, 99,6%) from Panreac. Triethoxysilylpropylmaleamic acid (TESPMA, 98%) was from Fluorochem. Triton® was provided from Supelco. Dulbecco's modified Eagle's medium (DMEM) was purchased from Lonza. 3-[4,5-Dimethylthiazolyl-2]-2,5-diphenyltetra-zolium bromide (MTT), penicillin G, streptomycin and glutamine solutions were purchased from Invitrogen.

Tetrahydrofuran (THF) and diethyl ether (Et_2O) were dried through PS-MD-2columns. Moisture sensitive reactions were carried out with magnetic stirring under an atmosphere of nitrogen in oven -or flame- dried glassware. Purification of reaction products was carried out by flash chromatography using silica gel 60 (230-400 mesh). Analytical thin layer chromatography was performed on 0.25 mm silica gel 60-F plates. Visualization was accomplished with UV light and phosphomolybdic acid-ammonium cerium (IV) nitric-sulfuric acid-water reagent, followed by heating.

2.2. Synthesis of cycloalkyne linker (1)

The 10-(2-cyclooctyn-1-oxy)-3-aza-5,8-dioxa-4-oxodecyl-1- amine linker 1 was prepared from 8,8-dibromobicyclo-[5.1.0]-octane [39]. Opening this bicyclic compound with diethyleneglycol in the presence of $AgBF_4$ afforeded the intermediate 2-[2-(cyclooct-2-yn-1-yloxy)ethoxy]ethanol, which was activated with DSC to 2-[2-(cyclooct-2-yn-1-yloxy)ethoxy]ethyl succini-midyl carbonate following the method of Riguera [40]. Finally, the product was reacted with ethylenediamine to provide the linker 1. Experimental details are disclosed in the Supporting Information (S1).

2.2. Synthesis of RGD azide ligand (2):

The H-Arg-Gly-Asp-NH-$(CH_2CH_2O)_3CH_2CH_2N_3$ RGD ligand 2 was prepared by the peptide coupling of Boc-Arg(Pbf)-GlyOH and H-Asp(OtBu)-NH-$(CH_2CH_2O)_3CH_2CH_2N_3$ fragments, followed by trifloroacetic-promoted removal of the protecting groups. The second fragment was, in its turn, synthesized from 1-amino-10-azido-3,6,9-trioxaundecane [41]. For experimental details, see Supporting Information (S2).

2.3. Synthesis of nanoparticles (Fe_3O_4 NPs)

The nanoparticles were synthesized by succesive additions of iron(0) pentacarbonyl in benzyl ether. A mixture of $Fe(CO)_5$ (3 mmol), 1,2-hexadecanediol (5 mmol), oleic acid (4 mmol), oleylamine (6 mmol) and benzyl ether (25 mL) were added to a three-necked flask. The reaction mixture was heated under mechanical stirring and a flow of argon gas until a temperature of 140 ºC was reached. This temperature was kept for 30 min and then the solution was heated to reflux (280 ºC) for 120 min. Successive additions to this solution of the iron pentacarbonyl precursor, oleic acid and oleylamine were performed in order to obtain different samples. In each step, the amount of iron precursor and ligands was calculated taking into account the desired size of the nanoparticles (Table S1). Subsequently, the solutions were cooled to room temperature. To remove the side products, ethanol was added to the reaction mixture and the resulting solution was centrifuged at 3500 rpm for 90 min. The formed nanoparticles were separated from the supernatant by centrifugation and the resultant solid was redispersed in a mixture of toluene and ethanol (5/10, v/v) to subsequently be separated by magnetic decantation. The cleaning process was repeated several times and the nanoparticles were finally suspended in toluene to obtain the solutions labeled as Fe_3O_4_A, Fe_3O_4_B, Fe_3O_4_C and Fe_3O_4_D.

Fe_3O_4_B_DMSA and Fe_3O_4_B_TESPMA nanoparticles.

The transfer of hydrophobic nanoparticles into aqueous media was performed replacing oleic acid ligands by hydrosoluble ones, such as dimercaptosuccinic acid (DMSA) and triethoxylsilylpropylmaleamic acid (TESPMA). In order to replace the superficial oleic acid with DMSA, a mixture of 20 mL toluene and a solution of 0,5 mmol DMSA in 5 mL DMSO was added to the particles, which were stirred mechanically (72 h). Solvent was then discarded, and precipitated particles were washed and centrifuged with ethanol. Finally,

nanoparticles were dispersed in alkaline H_2O and dialyzed before redispersion at pH 7. In the case of TESPMA functionalized nanoparticles, a solution of TESPMA in 10 mL AcOH/H_2O (0.1/10 v/v) and a solution of 8 mg Fe_3O_4 nanoparticles in 10 mL tetrahydrofuran was mixed during 24h. The resulting sample was washed and centrifuged three times with ethanol and redispersed in distilled H_2O. The hydrosoluble nanoparticles so obtained were labeled as Fe_3O_4_B_DMSA and Fe_3O_4_B_TESPMA.

Fe_3O_4_B_PMAO nanoparticles: The covering of nanoparticles with PMAO was performed using a modified protocol [42]. Accordingly, 28 mg of Fe_3O_4_B nanoparticles and the copolymer poly (maleic anhydride-alt-1-octadecene) were dissolved in chloroform (200 mL) at a mass ratio of 1:8. After vigorously stirring the solution for 1h, the solvent was slowly evaporated in a rotary evaporator, preventing the complete dryness of the sample. To get water-soluble nanoparticles, the hydrophilic anhydride groups present in the polymer were hydrolized by adding aqueous 0.1M NaOH (20 mL) and gently stirring the dispersion at 60 ºC. To remove the polymer excess, the particles were washed with distilled water on an ultracentrifuge at 24000rpm. The hydrosoluble nanoparticles so obtained were labeled as Fe_3O_4_B_PMAO.

Fe_3O_4_B_PMAO_PEG/RGD nanoparticles: The incorporation of RGD peptides to nanoparticles was conducted in two steps (Figure 1): first, the linker was anchored to the Fe_3O_4_B_PMAO carboxylic groups following a water-soluble carbodiimide protocol [43] and then the RGD ligand was clicked [44] to the intermediate Fe_3O_4_B_PMAO_cyOct nanoparticles. Thus, 10 μL of EDC (0.1 mg/mL) were added to 8 mg of nanoparticles dispersed in aqueous sodium tetraborate buffer (50 mM, pH = 9) to activate the carboxylic groups surface. Then, 0,001 mg of 10-(2-cyclooctyn-1-oxy)-3-aza-5,8-dioxa-4-oxodecyl-1-amine were added and the mixture was stirred at room temperature for 2 h. Surface charges were cancelled by adding 10 μL of NH_2PEG (0.1 mg/mL) to the suspension and the excess reagents were eliminated by centrifugal filtrations at 14000 r.p.m. The resulting Fe_3O_4_B_PMAO_PEGcyOct nanoparticles were treated with 0.1 mL of an aqueous 4.4 10^{-4} M solution of H-Arg-Gly-Asp-NH-$(CH_2CH_2O)_3CH_2CH_2N_3$ at 35°C for 2 h, after the mixture was sonicated for 1min. The “clicked” MNPs were thoroughly washed with distilled water to completely free the nanoparticles from reagents excess. The anchored NPs were labeled as Fe_3O_4_B_PMAO_PEG/RGD.

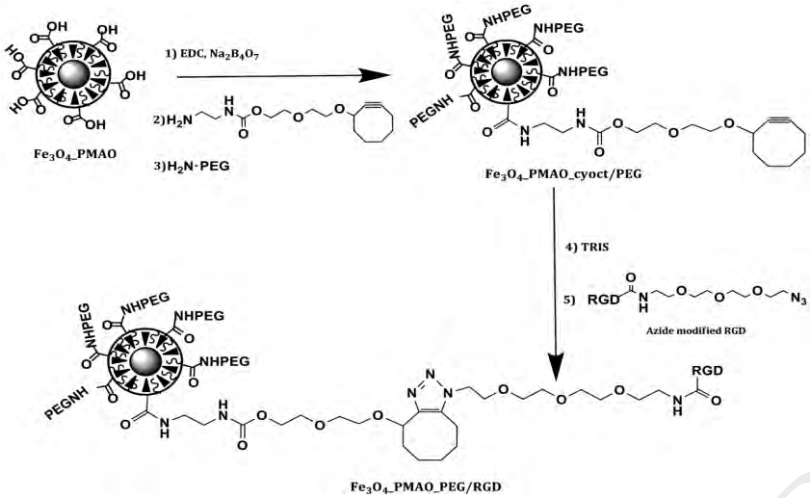

Figure 1. Schematic illustration of the synthesis of Fe_3O_4_B_PMAO_PEG/RGD nanoparticles.

2.4. Characterization

X-Ray Diffraction (XRD) of powder samples was recorded using using a PANalytical X'Pert PRO diffractometer equipped with copper anode (operated at 40 kV and 40 mA), diffracted beam monochromator and PIXcel detector. Scans were collected in the 5-70º 2θ range, with step size of 0,026º 2θ and 60 s per step. Thermogravimetric measurements were performed in a NETZSCH STA 449 C thermogravimetric analyser, by heating ≈ 10 mg of sample at 10°C/min under dry Ar atmosphere. The particle size and morphology was determined from TEM micrographs in a Philips CM200 microscope at an acceleration voltage of 200 KV. For preparing the samples, MNPs dispersed in toluene or water were dropped-cast onto copper grids.

Dynamic Light Scattering (DLS) measurements were carried out at 25°C with a Nano ZS (Malvern Instruments) equipped with a solid-state He-Ne laser (λ = 633 nm) to determine the hydrodynamic diameter of the hydrosoluble NPs. FTIR spectra of the nanoparticles and ligands were collected on a FTIR-8400S Shimadzu spectrometer in a 4000-400 cm^{-1} range and on a Bruker Alpha P. The measurements of magnetization versus temperature at 10 Oe were carried out in the temperature range of 5 and 300 K using a Quantum Design MPMS-7 SQUID magnetometer. Hysteresis loops at room temperature were done in a homemade VSM magnetometer up to a maximum field of 18 kOe with high low field resolution. Hysteresis loops at 5 K were performed in a VSM magnetometer from Cryogenic Ltd up to a maximum field of 100 kOe. EMR spectra were recorded on a Bruker ELESYS spectrometer, equipped

with a standard Oxford low-temperature device operating at X band; all measurements were carried out in toluene dispersions. Hyperthermia measurements were performed by a water-cooled induction coil machine designed in the Department of Electrical and Electronic of UPV/EHU, with varying field amplitude (0–30 kA/m) and at constant frequency of 532 and 676 KHz.

NMR spectra were recorded on a Bruker Avance-500 spectrometer at 500 MHz and 125 MHz frequencies for 1H and 13C nuclei, respectively. The chemical shifts are reported as δ values (ppm) relative to residual deuterated solvent as internal standards: for $CDCl_3$ δH (7.26 ppm) and δC (77.16 ppm), respectively.

Mass spectra were acquired on a time of flight (TOF) mass spectrometer (SYNAPT G2 HDMS from Waters, Milford, MA, USA) equipped with an electrospray source in positive mode (ESI+). Melting points were measured with a Büchi SMP-20 melting point apparatus and are uncorrected. Optical rotations were measured on a Jasco P-200 polarimeter using a sodium lamp (589 nm, D line) at 25 ±0.2 °C. The IR, 1H NMR and 13C NMR characterizations of organic materials and intermediate compounds synthesized are described in the Electronic Supporting Information of this article (S3).

2.5. Cytotoxicity assays

The cell viability was evaluated by a MTT assay, which measures the levels of the metabolically active mitochondrial dehydrogenase enzymes [45]. 5000 cells were seeded using a standard 96-well plate (TPP). After 24 hours of incubation in a humidified atmosphere containing 5% CO_2, the medium was replaced with new medium containing 6 different concentrations of Fe_3O_4_B_PMAO_PEG/RGD nanoparticles (0.01 – 0.5 mg mL^{-1}), a negative (without MNPs) and positive (cells treated with Triton X100) control. After 24 hours, the medium was replaced with fresh medium containing MTT dye solution to a final concentration of 0.5 mg mL^{-1} in DMEM. After 2 hours of incubation at 37 °C and 5% CO_2, the medium was eliminated and water-insoluble formazan was dissolved in 200 µL of DMSO. The absorbance was read on a microplate reader (Thermo Scientific Multiskan GO UV/Vis Microplate) at 570 nm. The relative cell viability (%) related to negative control wells containing cell without nanoparticles was calculated by [A]test/[A]controlx100.

3. Results and Discussion

3.1. Nanoparticles Preparation and Characterization

Succesive additions of iron pentacarbonyl in benzyl ether yield Fe_3O_4 NPs of different sizes, A, B, C and D, recovered by oleic acid. These hydrophobic nanoparticles were transferred to water by replacing oleic acid ligands by hydrosoluble ones, such as dimercaptosuccinic acid (DMSA) and triethoxylsilylpropylmaleamic acid (TESPMA) and Fe_3O_4_B_DMSA and Fe_3O_4_B_TESPMA samples were obtained. In other cases, the covering of nanoparticles with PMAO was performed and Fe_3O_4_B_PMAO samples were synthesized. These last ones were functionalized with RGD peptides and *Polyethylene glycol (PEG*). The incorporation of RGD peptides to nanoparticles was conducted in two steps: first, an hydrophilic w-aminoalkylcyclooctine linker and NH_2PEG were anchored to the carboxylic groups in Fe_3O_4_B_PMAO and then the RGD ligand was clicked to the intermediate Fe_3O_4_B_PMAO_cyOct nanoparticles to form Fe_3O_4_B_PMAO_PEG/RGD. The samples were characterized by means of X-Ray Diffraction (XRD), Infrared Spectroscopy (IR), Thermogravimetric analysis, Transmission Electron Microscopy (TEM) and Dynamic Light Scattering (DLS).

The XRD profiles of the firstly synthesized Fe_3O_4 NPs (A, B, C and D) confirmed the presence of nanocrystalline structures with quite broad diffraction peaks which positions and relative intensities match well with the standard profile of the characteristic spinel structure (LCPDS Nº 19-629) (Figure S1). From the full width at half maximum (FWHM) of the (3 1 1) diffraction peak average particle sizes were calculated by Scherrer's formula (Table 1, Table S2). Deconvolution of experimental (3 1 1) maxima for the different samples appear in Figure S2. The crystallite sizes varied in the 14–21 nm range and were related to the successive additions of metal precursors performed for increasing the sizes.

Particle size and crystallinity were also evaluated from TEM analysis. TEM micrographs exhibited monodisperse and faceted nanoparticles, except in the case of C sample (Figure 2). It could also be observed a tendency to a kind of self-assembling in A and B samples and a slight tendency to agglomeration in C and D samples, as morphology changed from cube-octahedral in A-B samples to more prismatic crystals in C-D samples. Also, it is worth emphasizing the anomalous wide size-dispersion found in C sample. The size analysis of these images fits to Gaussian profiles, and they are in the 10-23 nm range with dispersion

indices, defined as the ratio of standard deviation to mean diameter, between 1 and 4. The calculated d-spacings from electron diffraction patterns match well with those corresponding to magnetite (Fe_3O_4) (S.G.: F d3m). As shown in Table 1 mean sizes derived from TEM were in good accord with those calculated from XRD corroborating the conclusion that these nanoparticles are single crystals and discarding the appearance of twinning effects, as can be observed in Figure 2.

Although nanoparticles appear always well dispersed in toluene, when they are transferred to water different degrees of agglomeration can be observed, depending on the employed ligand. Fe_3O_4_B_TESPMA and Fe_3O_4_B_DMSA seem to agglomerate because of the low organic matter content on nanoparticles surface (Figure 2 (H, I)). TEM images of Fe_3O_4_B_PMAO show that they are still monodisperse with a narrow size distribution (Figure 2 (G)). In order to better define the degree of agglomeration of the water-soluble particles, DLS measurements were performed. The mean hydrodynamic diameter for toluene-dispersed Fe_3O_4_B NPs was 57.4 nm, a larger value than the 20 nm of NPs surrounded by oleic acid, which likely experienced some kind of aggregation. When replacing oleic acid by DMSA the hydrodynamic diameter maintains around 51.9 nm. Nevertheless, silane derived ligand, TESPMA, does not allow a complete dispersion of nanoparticles as hydrodynamic sizes over 700 nm are obtained, as can also be visualized by TEM measurements. In this case, additional interactions between TESPMA and other NPs and the lack of superficial charges could be the reasons for such kind of agglomeration. In the case of PMAO polymer coating, the hydrodynamic diameter for Fe_3O_4_B_PMAO and Fe_3O_4_B_PMAO_PEG/RGD are 78.0 and 111.1 nm, respectively. These values reflect the effect of the coating polymer layer on the 18 nm magnetic cores, together with a small degree of aggregation in the water-based colloid. The MNPs surface charges were assessed through measurements of the zeta potential of their aqueous suspensions. The values obtained are negative, being the most stable solutions Fe_3O_4_B_PMAO and Fe_3O_4_B_DMSA with –35.9 mV and -35.1 mV, respectively. Replacement by TESPMA or the incorporation of additional linkers decreased the stability to –20.3 mV and –15.5 mV, for Fe_3O_4_B_TESPMA and Fe_3O_4_B_PMAO_PEG/RGD, respectively. The lower values of the surface charge together with the increasing

hydrodynamic diameter for RGD covered NPs corroborate the addition of the peptide to the nanoparticles.

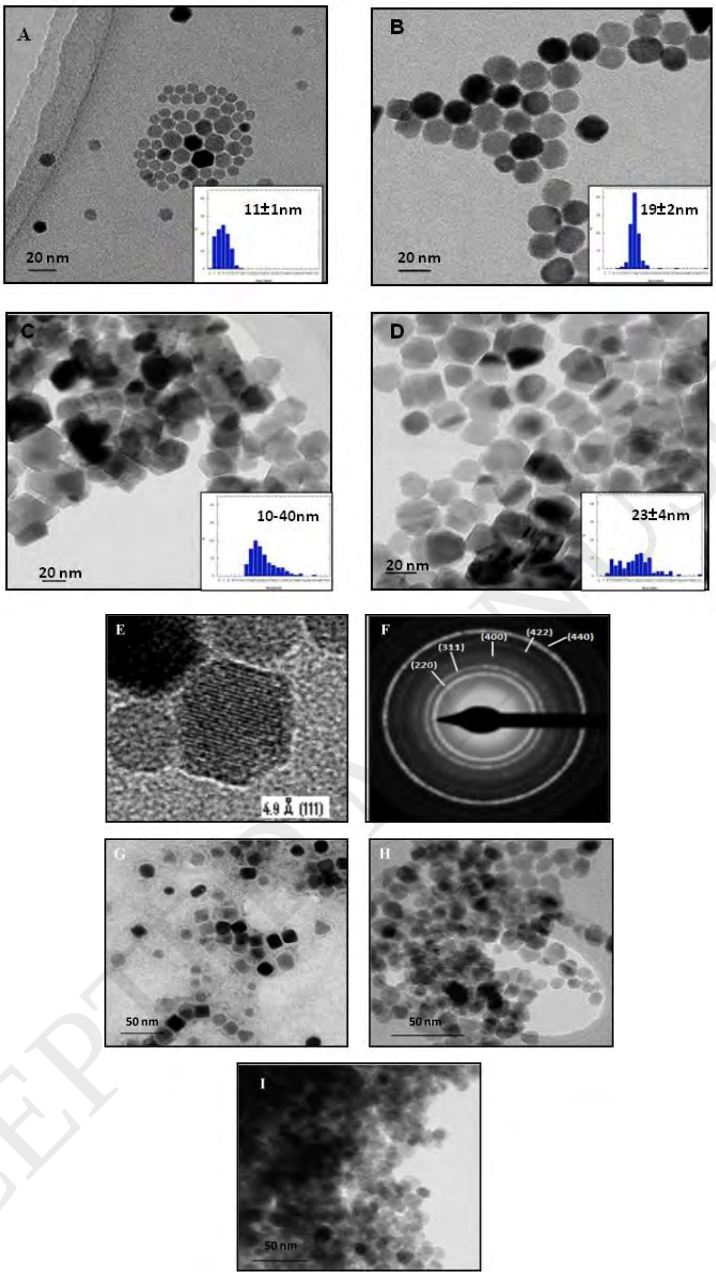

Figure 2. TEM images and size distributions of samples (A) Fe_3O_4_A, (B) Fe_3O_4_B, (C) Fe_3O4_C and (D) Fe_3O_4_D. Image of interplanar distances of sample Fe_3O_4_A (E) and indexed Electron Diffraction Pattern from selected area of sample Fe_3O_4_B (F). TEM images of (G) Fe_3O_4_B_PMAO, (H) Fe_3O_4_B_DMSA and (I) Fe_3O_4_B_TESPMA.

Infrared Spectroscopy measurements have been performed both on the ligands (oleic acid, DMSA, PMAO and TESPMA) and on functionalized magnetite nanoparticles in order to determine the prevailing capping agent and its absorption mechanisms on the particles surface (Figure S3). In the case of oleic acid recovered Fe_3O_4_B, the $–CH_2$ symmetric and asymmetric stretching vibrations at 2852 and 2920cm^{-1} reveal the presence of the oleyl group on the surface. This bonding pattern can be explained assuming a combination of molecules bonded symmetrically and forming an angle with the surface of nanoparticles [46]. Considering also that the absorption at 1053 cm^{-1} arises from C-O single bond stretching, it is clear that oleic acid is chemisorbed onto the Fe_3O_4 nanoparticles as a carboxylate. On the other hand, the band at 615 cm^{-1} is characteristic of Fe-O bonds in Fe_3O_4 [47]. In addition, the peaks at 1378 and 1601 cm^{-1} are assigned to the bidentate (–COO–Fe) mode of binding for oleic acid. Thus, these results are in good accord with the adsorption of carboxylate groups on nanoparticles surface. After coating with PMAO, stretching modes corresponding to C-O and C=O vibrations also appear at 1220 cm^{-1} and 1722 cm^{-1}, respectively. The band at 1722 cm^{-1} is attributed to the carboxyl groups in PMAO resulting from the opening of anhydride rings in PMAO. The silanization of the Fe_3O_4 nanoparticles surface with TESPMA was also identified by FTIR. The spectrum of Fe_3O_4_B_TESPMA shows absorption peaks at 2913 and 1415 cm^{-1}, which can be assigned to the stretching and bending modes in the alkyl chain. The peak at 1080 cm^{-1} corresponds to the Si-O bond on the Fe_3O_4 nanoparticle surface [48].[41] Finally, in the Fe_3O_4_B_DMSA spectrum, the low intensity band observed at 2504 cm^{-1} could be related to the S-H stretching vibrations [49].

The organic coating recovering magnetic nuclei has been calculated from TGA measurements performed in Ar atmosphere (Figure S4). The weight loss below 200°C is attributed to the evaporation of solvent remainders and adsorbed humidity. Between 200 °C and 700°C it may account for the mass loss of oleic acid and/or other organic ligands on the sample surface. Comparing the different nanoparticles covered by oleic acid, the ligand proportion greatly differs for the sample with the smallest size (Fe_3O_4_A), which presents a 31% of organic amount, mainly related with the greater superficial area. It can also be observed the increasing weight loss for PMAO covered sample comparing with TESPMA and DMSA covered ones, in good accord with a more effective recovering when employing the PMAO amphiphilic ligand.

3.2. *Magnetic Properties*

The characteristics detailed so far have a critical influence on the magnetic response of these nanoparticles, which were analyzed by DC Magnetometry and by EMR. The field dependence of Fe_3O_4_A, B, C and D were recorded at low (5 K) and room temperature (Figure 3) as diluted dispersions in order to minimize dipolar interactions. The absence of hysteresis at room temperature for Fe_3O_4 NPs points to a superparamagnetic-like behavior. However, the fine features of M(H) curves in Figure 3 reveal the existence of some significant deviations from the superparamagnetic state as the slope at low fields differs from SPM systems, leading to near-saturated curves at high fields. This deviation observed in large particles can be attributed to dipolar interaction effects, which are strongly sensitive to the total magnetic moment of the particles. Macroscopically such effects can be ascribed to a demagnetizing field which tends to tilt the curve M(H), so hindering the real susceptibility at low fields [50].

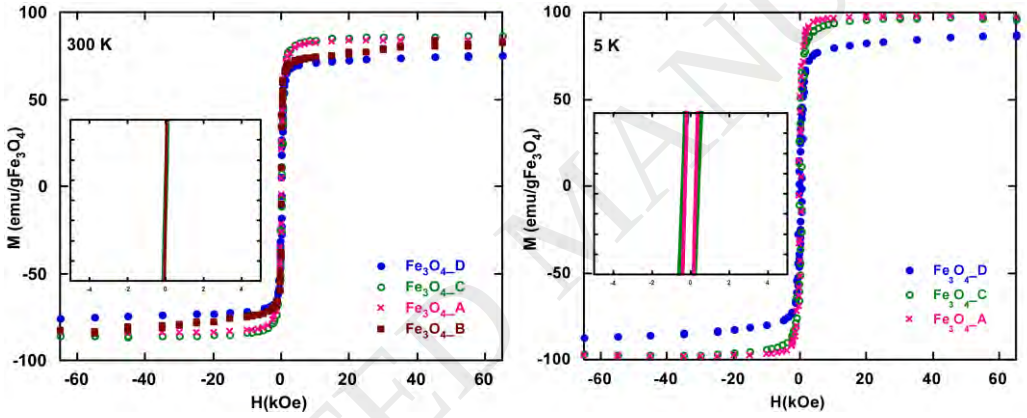

Figure 3. Experimental M vs H measurements at RT and 5K for Fe_3O_4_A, Fe_3O_4_B, Fe_3O_4_C, Fe_3O_4_D samples.

The saturation magnetization values (Table 1) obtained from the hysteresis loops at 300K (Figure 3), vary from 69.1 to 87.2 emu/gFe_3O_4, which slightly deviate from the bulk saturation value of magnetite (92 emu/g) [51]. This deviation could be ascribed to different effects as purity and crystallinity of the samples, the impact of surface spin disorder, which increases at high temperatures or to deviations from stoichiometric magnetite due to different occupancies of Fe(II), Fe(III) cations in T_d and O_h sites [52, 53]. At 5 K saturation magnetization are in good accord to the bulk value for magnetite. Coercive Field (H_c) values observed at 5 K (Figure 3) follow basically the expected trend for single magnetic domains:

the decrease of Hc with decreasing size, basically due to the progressive reduction of the anisotropy constant with size. However, in the case of Fe_3O_4_D nanoparticles (23 nm) H_c is shifted to the small value of 343 Oe, fact that could be related with inter-particle interactions appearing in the sample with nanoparticles above 25 nm and with less quantity of organic matter.

Measurements of magnetization versus temperature after Cooling at Zero Field (ZFC) and Field (FC) for colloidal samples dispersed in polystyrene are represented in Figure 4. Two different behaviours can be observed; Fe_3O_4_A and B NPs show the usual characteristics of a superparamagnetic behaviour, whose most distinctive feature is the increase of the blocking temperature (T_B) with the particle size, from 75 K in sample A to 92 K in sample B (table 1), and a progressive decrease of magnetization above T_B. It is to note in the case of Fe_3O_4_B the broadening of the maximum because of the strong dependence of T_B on diameter and on the dispersion of sizes. In the case of the larger samples (Fe_3O_4_D and C), a sharp feature at 107 K due to the Verwey transition is observed. Although this Verwey transition occurs at <120K in bulk magnetite, lower values (between 102 and 117K) are found in NPs, attributed to size effects [54,55].

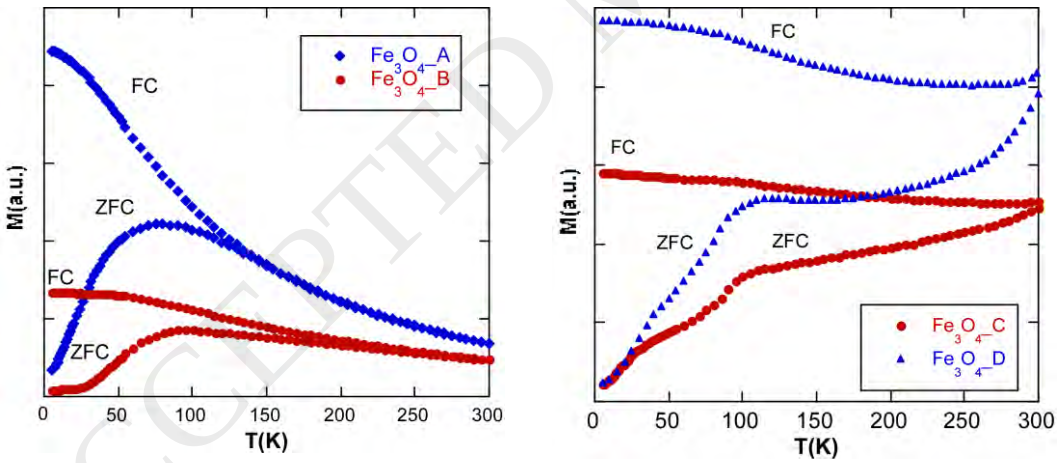

Figure 4. ZFC/FC curves for colloidal samples with an applied field of 10 Oe.

EMR measurements are not only crucial to complete microscopic magnetic characterization but has also been demonstrated its versatility for monitoring the degree of dispersion in the samples [56,57]. Spectra of the samples are represented in Figure 5 and they exhibit unique and well-resolved lines that become dependent on the degree of dilution due to the critical increase of interparticle dipolar interactions and/or the onset of strong aggregation effects.

These lines have been fitted to gaussian functions to determine the corresponding g-factors (Table 1). As can be observed, both the broadness of the line and the value of the resonant line, H_r, that is the g_{eff}, vary from one sample to another and are strongly correlated with nanoparticle size. Firstly, the g_{eff} shifts appreciably from 2 for all the samples, as only $g_{eff} = 2.0$ is observed for very small and homogeneous particles. Secondly, the g-factor increases sharply with diameter. In order to corroborate the previously observed exponential relation between sizes and g values, these data have been represented together with those from samples previously synthesized in the range of sizes 4.3 - 14.9 nm (Figure 5) [58,59]. Although some of the samples deviate slightly from the exponential curve, that is the case of samples with a broad size dispersion as Fe_3O_4_C, the dependence can be roughly observed. So, this exponential like correlation has proved to be quite useful and accurate in order to estimate sizes. In some cases, the existence of other magnetic contributions has also been observed, a fact related with the existence of multimodal distribution of sizes. It can also be noted that as nanoparticles' sizes increase, a greater distribution of sizes can be noticed and broader signals are observed. The appearance of this broadness is also related with the presence of dipolar interactions, which will be more intense for larger nanoparticles. In general, the bandwidth varies from 290 Gauss for Fe_3O_4_B, 420 Gauss (Fe_3O_4_A) and 730 Gauss (Fe_3O_4_D) to 2100 Gauss for Fe_3O_4_C, proving the higher degree of the size dispersions.

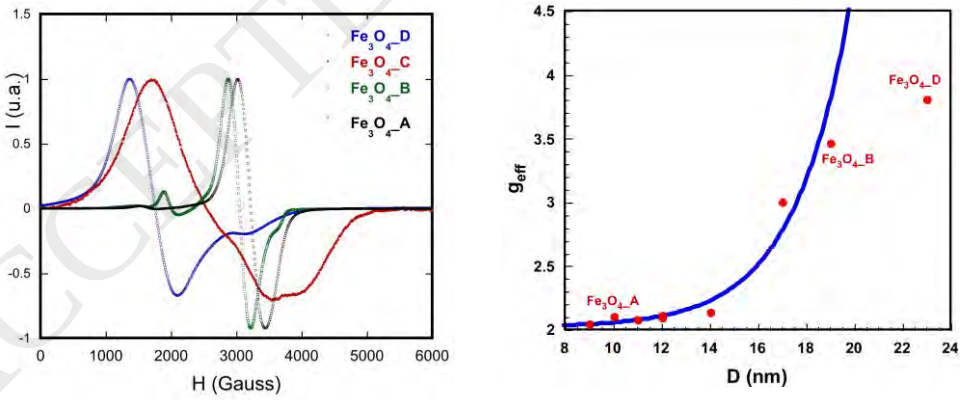

Figure 5. EMR measurements of Fe_3O_4_A, B, C and D (left) and g factor variation with nanoparticles sizes (right).

SAR values were measured by a lab-made AC magnetometer [60]. This device consists of an electromagnetic applicator based on an air-core inductor that generates the excitation AC

magnetic field. The inductor is part of a resonant LCC circuit feed by a power amplifier. The dynamic magnetization, M (t), is recorded thanks to two pick-up coils wound oppositely (Figure S5). Afterwards, the SAR values were obtained from the AC hysteresis loops area from 1 equation [61]:

$$SAR = \frac{f}{c}\mu_0 \oint M(t) \cdot dH_{app} \quad (1)$$

where M (*t*) is the instantaneous magnetization ($A \cdot m^{-1}$) at time t, H_{app} the field intensity ($A \cdot m^{-1}$) at time t, f (Hz) the applied magnetic field frequency and c ($mg\ Fe \cdot mL^{-1}$) the iron weight concentration. Note that in this case, the absorbed power was normalized to the iron concentration.

The SAR values were measured at different magnetic field frequencies (in the range of 149 - 1030 kHz) and at different magnetic field intensities (up to 21 $kA \cdot m^{-1}$). Figure 6 shows the so measured values for sample Fe_3O_4_A, Fe_3O_4_B, Fe_3O_4_C and Fe_3O_4_D. Clearly, sample Fe_3O_4_B presents the larger SAR values. However, the absorption rate of sample Fe_3O_4_C, the one with larger size nanoparticles, starts to rise rapidly above 10 $kA \cdot m^{-1}$. Regarding to sample Fe_3O_4_A, it presents the lower heating capabilities, in good agreement with its lower size (11 nm).

The so measured SAR values of sample Fe_3O_4_B dispersed in toluene and in water are alsso represented in Figure 6 at the same AC magnetic field frequency. Although similar values have been obtained, the water dispersed nanoparticles present higher SAR values at high fields intensities (above 5 $kA \cdot m^{-1}$). This fact can be ascribed to the higher viscosity of water comparing with toluene.

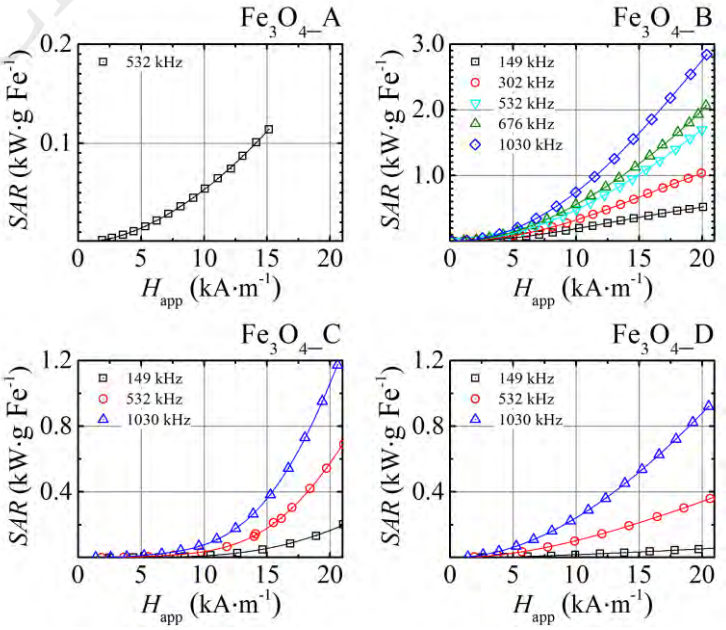

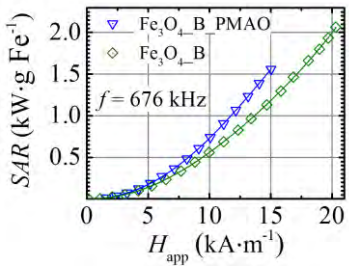

Figure 6. SAR values of toluene dispersed nanoparticle samples measured by AC magnetometry at different magnetic field intensities (H_{app}) and frequencies. Comparasion of toluene dispersed Fe_3O_4_B sample and water dispersed sample Fe_3O_4_B_PMAO at different magnetic field intensities (field frequency was 676 kHz).

3.3. Cytotoxicity assays

Since the novel nanoparticles prepared would eventually be applied as MRI contrast or magnetic hyperthermia agents in vivo assays, it was important to evaluate their biocompatibility. The cytotoxicity of Fe_3O_4_B_PMAO_PEG/RGD surface modified nanoparticles was tested in African green monkey kidney epithelial Vero cells, after 24 h incubation at different concentrations between 0.1 and 0.5 mg mL^{-1} of Fe (Figure 7). The cell viability was evaluated by a MTT assay, which measures the levels of the metabolically active mitochondrial dehydrogenase enzymes [45].

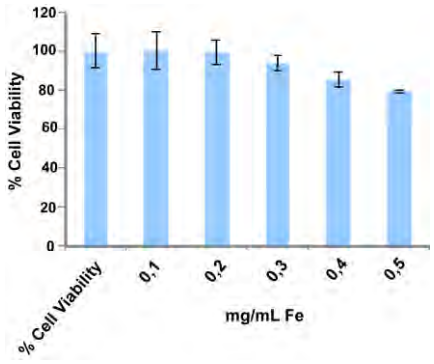

Figure 7. Cytotoxicity experiment for Fe_3O_4_B_PMAO_PEG/RGD sample, at different nanoparticle concentrations in Vero cells.

This preliminary in vitro cytotoxicity assay shows that Fe_3O_4_B_PMAO_PEG/RGD magnetite nanoparticles do not show significant cytotoxicity, even at 0.5 $mg.mL^{-1}$ concentration, as no meaningful changes are observed in the cell metabolic activity when compared with control cells. It is also remarkable that distilled water does not cause any decline in cell viability. Thus, this preliminary study reveals nontoxicity and biocompatibility of the synthesized nanoparticles.

4. Conclusions

The synthesis method of thermal decomposition by successive additions allowed obtaining samples of very high crystallinity without impurities with particle sizes between 11 and 27 nm. Water soluble nanoparticles have been obtained by ligand interexchange by means of DMSA and TESPMA and by adding the amphiphilic polymer PMAO. Moreover, a novel intelligent targeting system of magnetite NPs, Fe_3O_4_B_PMAO_PEG/RGD, was constructed by "click" anchoring of the RGD containing peptide on the surface of NPs via amide coupling. With the aid of the RGD moiety, these magnetic systems exhibited enhanced biocompatibility. The as-prepared nanoparticles showed biocompatibility and nontoxicity together with enhanced magnetic properties. In this sense, high values of SAR have been obtained for the nanoparticles, increasing with the mean size of the NPs and when nanoparticles are dispersed in water. So, these magnetite nanoparticles could be excellent candidates for biomedical applications such as hyperthermia treatments, being demonstrated that the Fe_3O_4_B_PMAO_PEG/RGD phase may present a great potential for cancer treatment. Actually, these nanoparticles are being applied in 'in vivo' experiments of magnetic hyperthermia in animals with induced colorectal tumours.

Notes

The authors declare no competing financial interest.

Acknowledgements

This work was supported by institutional funding from the Ministry of Economy and Competitiveness and Basque Government under Projects MAT2016-78266-P, FEDER, GIC-IT-570-13, Fondo Social de la DGA (grupos DGA), SAF2014-54763-C2-2-R. Technical and human support provided by SGIker (UPV/EHU) is also gratefully acknowledged. A grant from Gobierno Vasco to M.S.-A. (POS_2015_2-0048) is acknowledged.

REFERENCES

[1] B. Pelaz, S. Jaber, D. J. De Aberasturi, V. Wulf, T. Aida, J. M. de la Fuente, J. Feldmann, H. E. Gaub, L. Josephson, C. R. Kagan, N. A. Kotov, L. M. Liz-Marzán H. Mattoussi, P. Mulvaney, C. B. Murray, , A. L. Rogach, P. S. Weiss, I. Willner and W. J. Parak, The state of nanoparticle-based nanoscience and biotechnology: progress, promises, and challenges. ACS Nano 6 **(2012)** 8468–8483.

[2] G. F. Goya, V. Grazú and M. R. Ibarra, Magnetic nanoparticles for cancer therapy. Curr. Nanosci. 4 (2008) 1–16.

[3] A. Meffre, B. Mehdaoui, V. Kelsen, P. F. Fazzini, J. Carrey, S. Lachaize, M. Respaud and B. Chaudret, A simple chemical route toward monodisperse iron carbide nanoparticles displaying tunable magnetic and unprecedented hyperthermia properties. Nano Lett. 12 (2012) 4722–4728.

[4] J. P. Fortin, C. Wilhelm, J. Servais, C. Ménager, J. C. Bacri and F. Gazeau, Size-sorted anionic iron oxide nanomagnets as colloidal mediators for magnetic hyperthermia. J. Am. Chem. Soc. 129 (2007) 2628–2635.

[5] P. B. Santhosh and N. P. Ulrih, Multifunctional superparamagnetic iron oxide nanoparticles: promising tools in cancer theranostics. Cancer Lett. 336 (2013) 8–17.

[6] S. A. Jadhav and R. Bongiovanni, Synthesis and organic functionalization approaches for magnetite (Fe3O4) nanoparticles. Adv. Mat. Lett. 3 (2012) 356–361.

[7] M. A. Gonzalez-Fernandez, T. E. Torres, M. Andrés-Verges, R. Costo, P. de la Presa, C. J. Serna, M. P. Morales, C. Marquina, M. R. Ibarra and G. F. Goya, Magnetic nanoparticles for power absorption: Optimizing size, shape and magnetic properties. J. Solid State Chem. 182 (2009) 2779–2784.

[8] N.R. Jana,Y. Chen, X. Peng, Size- and shape-controlled magnetic (Cr, Mn, Fe, Co, Ni) oxide nanocrystals via a simple and general approach. Chem. Mater. 16 (2004) 3931–3935.

[9] M. C. Bautista, O. Bomati-Miguel, M. del Puerto Morales, C. J. Serna and S. Veintemillas-Verdaguer, Surface characterisation of dextran-coated iron oxide nanoparticles prepared by laser pyrolysis and coprecipitation. J. Magn. Magn. Mater. 293 (2005) 20–27.

[10] A. K. Hauser, R. Mathias, K. W. Anderson and J. Zach Hilt, The effects of synthesis method on the physical and chemical properties of dextran coated iron oxide nanoparticles. Mater. Chem. Phys. 160 (2015) 177–186.

[11] W. Zhang, S. Jia, Q. Wu, S. Wu, J. Ran, Y. Liu and J. Hou, Studies of the magnetic field intensity on the synthesis of chitosan-coated magnetite nanocomposites by co-precipitation method. *Mater. Sci. Eng. C* 32 (2012) 381–384.

[12] Y. Ding, S. Z. Shen, H. Sun, K. Sun, F. Liu, Y. Qi and J. Yan, Design and construction of polymerized-chitosan coated Fe3O4 magnetic nanoparticles and its application for hydrophobic drug delivery. *Mater. Sci.Eng. C* 48 (2015) 487–498.

[13] M. Anbarasu, M. Anandan, E. Chinnasamy, V. Gopinath and K. Balamurugan, Synthesis and characterization of polyethylene glycol (PEG) coated Fe3O4 nanoparticles by chemical co-precipitation method for biomedical applications. *Spectrochim. Acta. A* 135 (2015) 536–539.

[14] E. Illés, E. Tombácz, M. Szekeres, I. Y. Tóth, Á. Szabó and B. Iván, (2015) Novel carboxylated PEG-coating on magnetite nanoparticles designed for biomedical applications. *J. Magn. Magn. Mater.* 380, 132–139.

[15] E. Ranjbakhsh, A. K. Bordbar, M. Abbasi, A. R. Khosropour and E. Shams, Enhancement of stability and catalytic activity of immobilized lipase on silica-coated modified magnetite nanoparticles. *Chem. Eng. J.* 179 (2012) 272–276.

[16] M. Ma, Y. Zhang and W. Yu, Preparation and characterization of magnetite nanoparticles coated by amino silane. *Colloid Surface A* 212 (2003) 219–226.

[17] W. W. Yu, E. Chang, C. M. Sayes, R. Drezek and V. L. Colvin, Aqueous dispersion of monodisperse magnetic iron oxide nanocrystals through phase transfer. *Nanotech.* 17 (2006) 4483–4487.

[18] K. Hola, Z. Markova, G. Zoppellaro, J. Tucek and R. Zboril, Tailored functionalization of iron oxide nanoparticles for MRI, drug delivery, magnetic separation and immobilization of biosubstances. *Biotechnol. Adv.* 33 (2015) 1162–1176.

[19] X. L. Liu and H. M. Fan, Innovative magnetic nanoparticle platform for magnetic resonance imaging and magnetic fluid hyperthermia applications. *Curr. Opin. Chem. Eng.* 4 (2014) 38–46.

[20] E. Ruoslahti, Peptides as targeting elements and tissue penetration devices for nanoparticles. *Adv. Mater.* 24 (2012) 3747–3756.

[21] D. Arosio, L. Manzoni, E. M. V Araldi and C. Scolastico, Cyclic RGD functionalized gold nanoparticles for tumor targeting. Bioconjugate Chem. 22 (2011) 664–672.

[22] E. Ruoslahti, RGD and other recognition sequences for integrins. Annu. Rev. Cell Dev. Biol. 12 (1996) 697–715.

[23] J. M. de la Fuente, C. C. Berry, M. O. Riehle and A. S. G. Curtis, Nanoparticle targeting at cells Langmuir 22 (2006) 3286–3293.

[24] M. Das, D. Bandyopadhyay, D. Mishra, S. Datir, P. Dhak, S. Jain, T. K. Maiti, A. Basak and P. Pramanik, "Clickable", Trifunctional magnetite nanoparticles and their chemoselective biofunctionalization. Bioconjugate Chem. 22 (2011) 1181–1193.

[25] A. Cardiel, B. Michelle, L. Bishop, K. Louis, J. Yeager, Y. Tan and R. Hames, Chemically directed assembly of photoactive metal oxide nanoparticle heterojunctions via the copper-catalyzed azide–alkyne cycloaddition "click" reaction. ACS Nano 6 (2012) 310–318.

[26] M. Meldal and C. W. Tornøe, Cu-catalyzed azide-alkyne cycloaddition. Chem. Rev. 108 (2008) 2952–3015.

[27] C. Palomo, J. M. Aizpurua, E. Balentová, I. Azcune, J. Ignacio, J. Jiménez-Barbero, F. J. Cañada and J. I. Miranda, "Click" saccharide/β-lactam hybrids for lectin inhibition. Org. Lett. 10 (2008) 2227–2230.

[28] N. J. Agard, J. A. Prescher and C. R. Bertozzi, A strain-promoted [3 + 2] azide−alkyne cycloaddition for covalent modification of biomolecules in living systems J. Am. Chem. Soc. 126 (2004) 15046–1547.

[29] J. C. Jewett and C. R. Bertozzi, Cu-free click cycloaddition reactions in chemical biology. Chem. Soc. Rev. 39 (2010) 1272–1279.

[30] M. Levy, A. Quarta, A. Espinosa, A. Figuerola, C. Wilhelm, M. García-Hernández, A. Genovese, A. Falqui, D. Alloyeau, R. Buonsanti, P. D. Cozzoli, M. A. García, F. Gazeau and T. Pellegrino, Correlating magneto-structural properties to hyperthermia performance of highly monodisperse iron oxide nanoparticles prepared by a seeded-growth route. Chem. Mater. 23 (2011) 4170–4180.

[31] L. Zhang, R. He and H. C. Gu, Synthesis and kinetic shape and size evolution of magnetic nanoparticles. Mater. Res. Bull. 41 (2006) 260–267.

[32] P. Guardia, R. Di Corato, L. Lartigue, C. Wilhelm, A. Espinosa, M. García-Hernández, F. Gazeau, L. Manna and T. Pellegrino, Water-soluble iron oxide nanocubes with high values of specific absorption rate for cancer cell hyperthermia treatment. ACS Nano 6 (2012) 3080–3091.

[33] R. Mejías, S. Pérez-Yagüe, L. Gutiérrez, L. I. Cabrera, R. Spada, P. Acedo, C. J. Serna, F. J. Lázaro, A. Villanueva, M. D. P. Morales and D. F. Barber, Dimercaptosuccinic acid-coated magnetite nanoparticles for magnetically guided in vivo delivery of interferon gamma for cancer immunotherapy. Biomaterials 32 (2011) 2938–2952.

[34] Y. Kurihara, M. Takama, T. Sekiya, Y. Yoshihara, T. Ooya and T. Takeuchi, Fabrication of carboxylated silicon nitride sensor chips for detection of antigen–antibody reaction using microfluidic reflectometric interference spectroscopy. Langmuir 28 (2012) 13609–13615.

[35] W. J. Parak, C. J. Lin, R. A. Sperling, J. K. Li, T. Y. Yang, P. Y. Li, M. Zanella and W. H. Chang,. Design of an amphiphilic polymer for nanoparticle coating and functionalization. Small 4 (2008) 334–341.

[36] Z. Monasterio, M. Sagartzazu-Aizpurua, J. I. Miranda, Y. Reyes and J. M. Aizpurua, Cationic 1,2,3-triazolium alkynes: components to enhance 1,4-regioselective azide–alkyne cycloaddition reactions. Org. Lett. 18 (2016) 788–791.

[37] N. Noginova, T. Weaver, E. P. Giannelis, a. B. Bourlinos, V. A. Atsarkin and V. V. Demidov, Observation of multiple quantum transitions in magnetic nanoparticles. Phys. Rev. B - Condens. Matter Mater. Phys. 77 (2008) 1–5.

[38] M. Yulikov, P. Lueders, M. Farooq Warsi, V. Chechik and G. Jeschke, Distance measurements in Au nanoparticles functionalized with nitroxide radicals and Gd(3+)-DTPA chelate complexes. Phys. Chem. Chem. Phys. 14 (2012) 10732–10746.

[39] A. Bernardin, A. Cazet, L. Guyon, P. Delannoy, F. Vinet, D. Bonnafee and I. Texier, Copper-free click chemistry for highly luminescent quantum dot conjugates: application to in vivo metabolic imaging. Bioconjugate Chem. 21 (2010) 583–588.

[40] E. Lallana, E. Fernandez-Megia and R. Riguera, Surpassing the use of copper in the click functionalization of polymeric nanostructures: a strain-promoted approach. J. Am. Chem. Soc. 131 (2009) 5748–5750.

[41] M. Gonçalves, K. Estieu-Gionnet, T. Berthelot, G. Laïn, M. Bayle, X. Canron, N. Betz, A. Bikfalvi and G. Déléris, Design, synthesis, and evaluation of original carriers for targeting vascular endothelial growth factor receptor interactions. Pharm. Res. 22 (2005) 1411–1421.

[42] R. Di Corato, A. Quarta, P. Piacenza, A. Ragusa, A. Figuerola, R. Buonsanti, R. Cingolani, L. Manna and T. Pellegrino, Water solubilization of hydrophobic nanocrystals by means of poly(maleic anhydride-alt-1-octadecene). J. Mater. Chem. 18 (2008) 1991–1996.

[43] N. Nakajima and Y. Ikada, Mechanism of amide formation by carbodiimide for bioconjugation in aqueous media. Bioconjugate Chem. 6 (1995) 123–130.

[44] J. Bolley, E. Guenin, N. Lievre, M. Lecouvey, M. Soussan, Y. Lalatonne and L. Motte, Carbodiimide versus click chemistry for nanoparticle surface functionalization: a comparative study for the elaboration of multimodal superparamagnetic nanoparticles targeting αvβ3 integrins. Langmuir 29 (2013) 14639–14647.

[45] T. Mosmann, Rapid colorimetric assay for cellular growth and survival: application to proliferation and cytotoxicity assays. *J. Immunol. Methods* 65 (1998) 55–63.

[46] Nakamoto, K. (1978) *Infrared and raman spectra of inorganic and coordination compounds* (New York: Wiley).

[47] H. Qu, D. Caruntu, H. Liu and C. J. O'Connor, Water-dispersible iron oxide magnetic nanoparticles with versatile surface functionalities. *Langmuir* 27 (2011) 2271–2278.

[48] S. Hozhabr Araghi and M. H. Entezari, Amino-functionalized silica magnetite nanoparticles for the simultaneous removal of pollutants from aqueous solution. *Appl. Surf. Sci.* 333 (2015) 68–77.

[49] Z. P. Chen, Y. Zhang, S. Zhang, J. G. Xia, J. W. Liu, K. Xu and N. Gu, Preparation and characterization of water-soluble monodisperse magnetic iron oxide nanoparticles via surface double-exchange with DMSA. *Colloid Surface A* 316 (2008) 210–216.

[50] K. Mandal, S. Mitra and P. A. Kumar, Deviation from Bloch T3/2 law in ferrite nanoparticles. *Europhys. Lett.* 75 (2006) 618–623.

[51] B. D. Cullity, *Introduction to magnetic materials* (Masssachusetts: Addison-Wesley) (1972).

[52] X. Batlle, N. Pérez, P. Guardia, O. Iglesias, A. Labarta, F. Bartolomé, L. M. Garca, J. Bartolomé, A. G. Roca, M. P. Morales and C. J. Serna, Magnetic nanoparticles with bulklike properties. *J. App. Phys*. 109 (2011) 07B524–07B526.

[53] V.S. Coker, C·I. Pearce, C. Lang, G.V. Laan, R·A.D. Pattrick, N·D. Telling, D· Schüler, E· Arenholz and J·R. Lloyd, Cation site occupancy of biogenic magnetite compared to polygenic ferrite spinels determined by X-ray magnetic circular dichroism. *Eur. J. Miner*. 19 (2007) 707.

[54] M.L. Fdez-Gubieda, A. Muela, J. Alonso, A. García, M. Barandiara, R. Ferna, Magnetite biomineralization in magnetospirillum gryphiswaldense: time-resolved magnetic and structural studies. *ACS Nano* 7 (2013) 3297–3305.

[55] J.P. Sheperd, R. Aragan, J. W. Koenitzer, J. M. Honig, Changes in the nature of the verwey transition in nonstoichiometric magnetite (Fe3O4). *Phys. Rev. B* 32 (1985) 1818–1819.

[56] P. Ceci, E. Chiancone, O. Kasyutich, G. Bellapadrona, L. Castelli, M. Fittipaldi, D. Gatteschi, C. Innocenti and C. Sangregorio, Synthesis of iron oxide nanoparticles in listeria innocua Dps (DNA-binding protein from starved cells): a study with the wild-type protein and a catalytic centre mutant. *Chem. - A Eur. J.* 16 (2010) 709–717.

[57] J. Salado, M. Insausti, L. Lezama, I. Gil de Muro, E. Goikolea and T. Rojo, Preparation and characterization of monodisperse Fe3O4 nanoparticles: an electron magnetic resonance study. *Chem. Mater*. 23 (2011) 2879–2885.

[58] I. Castellanos-Rubio, M. Insausti, E. Garaio, I. Gil de Muro, F. Plazaola, T. Rojo and L. Lezama, Fe3O4 nanoparticles prepared by the seeded-growth route for hyperthermia: electron magnetic resonance as a key tool to evaluate size distribution in magnetic nanoparticles. *Nanoscale* 12 (2014) 7542–7552.

[59] M. Junk, *Assessing the Functional Structure of Molecular Transporters by EPR Spectroscopy* (Mainz: Springer) (2012).

[60] E. Garaio, J. M. Collantes, F. Plazaola, J. A. Garcia and I. Castellanos-Rubio, A multifrequency eletromagnetic applicator with an integrated AC magnetometer for magnetic hyperthermia experiments. *Meas. Sci. Technol.* 25 (2014) 115702.

[61] E. Garaio, J. M. Collantes, J. A. Garcia, F. Plazaola, S. Mornet, F. Couillaud and O. Sandre, A wide-frequency range AC magnetometer to measure the specific absorption rate in nanoparticles for magnetic hyperthermia. *J. Magn. Magn. Mater*. 368 (2014) 432–437.

Table 1. Particle average diameter measured by TEM (D_{TEM}) and XRD (D_{XRD}), organic content, saturation magnetization at 300K (M_S and blocking temperature (T_B) determined by FC-ZFC curve, g effective value measured by EMR and SAR values of the NP samples**.**

Sample	D(nm) XRD	D(nm) /β TEM	% organic matter	M_S(emu/g)* 300 K	T_B(K)	g_{eff}	*SAR* (532kHz, 15kA/m)
Fe_3O_4_A	11	11±1	31.1	87.2	80.1	2.1	113
Fe_3O_4_B	18	19±2	18.7	75.2	90.8	2.2	695
Fe_3O_4_C	27	10-40	19.1	85.9	105.1	2.6	200
Fe_3O_4_D	23	23±4	17.0	69.1	111.7	3.8	213